# Amplified Mesoscale and Submesoscale Variability and Increased Concentration of Precipitation under Global Warming over Western North America

CLÉMENT GUILLOTEAU,[a] XIAODONG CHEN,[b,d,e] L. RUBY LEUNG,[b] AND EFI FOUFOULA-GEORGIOU[a,c]

[a] *Department of Civil and Environmental Engineering, University of California, Irvine, Irvine, California*
[b] *Atmospheric, Climate and Earth Sciences Division, Pacific Northwest National Laboratory, Richland, Washington*
[c] *Department of Earth System Science, University of California, Irvine, Irvine, California*
[d] *School of Meteorology, University of Oklahoma, Norman, Oklahoma*
[e] *School of Civil Engineering and Environmental Science, University of Oklahoma, Norman, Oklahoma*

(Manuscript received 18 June 2024, in final form 3 February 2025, accepted 18 February 2025)

ABSTRACT: Cold-season precipitation statistics in simulations from the storm-resolving WRF Model at 6-km and 1-h resolution over western North America are analyzed. Pseudo–global warming future simulations for the 2041–80 period, constrained by GCMs under the RCP8.5 scenario, are compared to the 1981–2020 historical simulation. The analysis focuses on the dynamical properties of precipitation time series at subdaily scales and on the morphology of storms. The statistical distribution of precipitation intensities in each pixel of the simulation domain is characterized through nonparametric statistical indicators: frequency of wet hours, mean wet-hour precipitation intensity, and Gini coefficient as a measure of the temporal concentration of the precipitation volume. Additionally, the temporal and spatial Fourier power spectra of precipitation time series and precipitation fields are analyzed. The half-power period (HPP) and half-power wavelength (HPW) are defined as spectral measures of the characteristic scales of precipitation's temporal and spatial patterns. The results show statistically significant increases in the mean wet-hour precipitation intensity and in the Gini coefficient in 99% of the pixels, indicating that the seasonal precipitation volume becomes more concentrated within a smaller number of hours with higher precipitation intensity. The statistics of change in the frequency of wet hours are more contrasted across the simulation domain. The changes are also reflected in the power spectra, which show the spatial and temporal variability increasing proportionally more with finer spatial and temporal scales and the HPW and HPP decreasing. These projected changes are expected to have consequences, not only in terms of hydrologic impacts but also in terms of the predictability of precipitation patterns.

SIGNIFICANCE STATEMENT: The precipitation characteristics of winter storms over the western United States and southwestern Canada are analyzed in future climate simulations for the 2041–80 period. As compared to present-day climate, the most intense parts of the storms are projected to produce a higher rainfall volume, with increased concentration over smaller areas and shorter time intervals. The propensity of rainfall intensity to vary rapidly over time will be enhanced in the future according to the simulations. These model predictions imply an increased risk of rapid flooding in small basins. They also suggest that predicting several hours ahead the time and location at which a storm will produce maximum rainfall may become more challenging in the future.

KEYWORDS: Precipitation; Climate change; Climate prediction; Model output statistics; Deep convection

## 1. Introduction

Change in precipitation under global warming is expected to manifest in a complex way: Beyond changes in the mean annual precipitation volume, changes in the frequency of storms, the frequency of extreme high values, the duration of wet spells and dry spells, the magnitude and timing of the diurnal cycle, seasonal cycle, and the multiannual cycles such as ENSO may occur. At the storm level, statistics regarding the spatial extent, geometrical properties, trajectory, and dynamics of storms may also be changing. A large volume of literature covering all these different aspects has already been published, reporting statistics derived from a wide range of different approaches and metrics, applied to different datasets (e.g., O'Gorman 2015; Pascale et al. 2016; Donat et al. 2016; Pfahl et al. 2017; Swain et al. 2018; Liu et al. 2019; Giorgi et al. 2019; Mamalakis et al. 2021; Thackeray et al. 2022; Chan et al. 2023; Chen et al. 2023; Abdelmoaty and Papalexiou 2023). While this rich literature, comprising global, regional, and local analyses, provides a thorough far-reaching understanding of change in precipitation under global warming, a synthesis of consistent findings has still to be reached (Zaitchik et al. 2023).

The Clausius–Clapeyron relationship, which determines the saturation vapor pressure of water in the air as a function of the temperature, establishes that the water-holding capacity of the atmosphere increases by 7% for every 1-K increase in temperature. While constraints on Earth's energy budget confine the increase in the global precipitation volume to a much lower rate (between 1% and 3% for every 1 K), the increase in the intensity of high precipitation extremes may actually follow the 7%/K rate and even surpass it (Berg et al. 2013;

Supplemental information related to this paper is available at the Journals Online website: https://doi.org/10.1175/JCLI-D-24-0343.s1.

*Corresponding author*: Clément Guilloteau, cguillot@uci.edu

DOI: 10.1175/JCLI-D-24-0343.1

Westra et al. 2014; Lenderink et al. 2017; Fowler et al. 2021). This change in extreme statistics beyond the Clausius–Clapeyron relationship is associated with changes in the dynamics, organization, and morphology of precipitation systems and in convective precipitation systems in particular.

Evaluating storm morphology and subdaily dynamics in numerical simulations of historical and future climates requires that these simulations explicitly resolve individual storms with adequate spatial and temporal resolutions (typically 1-h or finer temporal resolution and spatial resolutions no coarser than 10 km). Such simulations are extremely computationally expensive to run over large domains and over long periods. Global storm-resolving simulations at such resolutions can generally simulate only a few months' worth of data at the cost of several million CPU hours (Stevens et al. 2019; Takayabu et al. 2022; Kendon et al. 2021). When comparing climate simulations under historical and future conditions, the simulated periods must be long enough to account for internal variability. This is particularly true when the comparison focuses on rare events. We note that, at hourly and kilometric resolutions, the occurrence of precipitation can be considered a statistically rare event, as, in most regions of the world, less than 20% of hours are precipitating hours (Venugopal and Wallace 2016), and most of the annual precipitation is in fact brought by no more than 30 storm events each year (Goffin et al. 2024). To obtain a reasonable sample size of simulated storms for robust statistical analyses, one must therefore consider simulations covering periods of several years. Moreover, if one wants to average out the effect of multiannual climate cycles such as ENSO, the simulated period should reasonably cover several decades. At the moment, storm-resolving simulations covering several decades are only available at the regional scale (Lucas-Picher et al. 2021).

In the present study, we analyze high-resolution (1 h, 6 km) numerical simulations for 40 years of historical and 40 years of future climate conditions in western North America, to study changes in the cold-season (October–March) spatiotemporal patterns of precipitation with emphasis on the mesoscales (spatial scales ranging from 20 to 200 km) and submesoscales (spatial scales finer than 20 km) and on the subdaily temporal variability. These simulations have been generated under the Strategic Environmental Research and Development Program funded by the U.S. Department of Defense to investigate future changes in precipitation intensity–duration–frequency in military installations in the western United States and under the HyperFACETS project (Framework for Improving Analysis and Modeling of Earth System and Intersectoral Dynamics at Regional Scales) funded by the Department of Energy to evaluate the scientific credibility of models for decision-making, with focus on simulating the western North American hydroclimate and the influence of complex topography. This unique set of simulations is one of the very few existing storm-resolving simulation datasets covering several decades over an area of several million square kilometers, for both historical and future climate. The present analysis builds upon and expands the analyses by Chen et al. (2018, 2019, 2023) and Koszuta et al. (2024), focusing on the changing characteristics of precipitation in western North America under global warming.

Beyond the abovementioned projects, the western North America area has been the focus of several recent publications dealing with changes in precipitation characteristics under global warming (e.g., Liu et al. 2017; Huang et al. 2020; Gensini et al. 2023; Rahimi et al. 2024). With the frequent occurrence of atmospheric rivers during the cold season (Rutz et al. 2014; Gershunov et al. 2019), western North America is particularly exposed to hazards induced by intense precipitation occurring over durations (a few hours) such as flash floods, landslides, and debris flow (Ralph and Dettinger 2011; Cordeira et al. 2019; Guilinger et al. 2023). The typical cold-season atmospheric rivers occurring in western North America can be classified as mesoscale convective systems or mesoscale convective complexes with pronounced spatial anisotropy. An atmospheric river typically produces intense precipitation over a narrow band; while its length may extend over distances up to 2000 km, the width of the rainband is generally on the order of 100–300 km. As convective systems, atmospheric rivers show strong spatial variability at mesoscale and submesoscale, with individual convective cells within atmospheric rivers having typical dimensions of a few kilometers to a few dozen kilometers. Also, while, as a mesoscale system/complex, an atmospheric river may last for up to 2 or 3 days, individual convective cells within the system may develop and decay within periods of a few hours. Thus, spatially localized patterns of extreme precipitation intensities over short time periods within atmospheric river systems are of particular importance in terms of hydrological impacts and hazards.

Classically, high extremes are defined as values above a certain quantile (95th and 99th percentiles being often chosen). From such a definition, several issues may arise. First, the selection of a specific quantile is always partially arbitrary, as the definition of an extreme value varies depending on the data user and the targeted application (Pendergrass 2018; VanBuskirk et al. 2021). The results of studies for which different quantiles have been chosen to define extreme values are not easily compared or compiled together. Alternatively, the statistical analysis of extremes can be performed using a parametric representation of the distribution of precipitation intensities. Here again, different choices made in terms of parameterization make different studies hardly comparable with each other. Moreover, either with quantile-based approaches or with parametric approaches, a critical element in statistical studies of extremes is the scale dependence of the statistics. Indeed, extreme analyses conducted at different scales (e.g., seasonal scale, daily scale, and hourly scale) can hardly be compared with each other because the statistical distribution of precipitation rates can change drastically from one scale to another. At subhourly and kilometric resolutions, measured precipitation intensities show a high fraction of zeros and a skewed heavy-tail distribution for above-zero intensities. At coarser scales, the fraction of zeros decreases and the skewness of the distribution reduces. Therefore, a suitable parametric representation of the distribution of precipitation intensities at one scale may be unsuitable at another scale, and the interpretation of a certain quantile value as an extreme at a given scale may not hold at another scale.

When it comes to evaluating storm morphology and dynamics, many studies rely on object extraction, either in precipitation time series or in multidimensional (spatial or spatiotemporal) precipitation fields, an object being a continuous/coherent feature localized and delimited in space and time, as, for example, a storm, a storm complex, a convective cell, or a cluster of convective cells within a storm (e.g., Guinard et al. 2015; Ferreira et al. 2018; Chen et al. 2023). Here again, results can be highly sensitive to the way objects are defined and the parametric choices (in particular to the thresholds chosen for object extraction). Object-based metrics are therefore case specific and not easily comparable across different studies. Such methods are not always fully automatable and generally require human supervision and fine parametric tuning, making them cumbersome to apply on large datasets or across multiple datasets.

The present study relies on the use of nonparametric metrics that do not require subjective selection of thresholds and that can be easily computed over large regions, long periods of time, and across multiple datasets, in contrast to the cumbersome and subjective object extraction methodologies. Changes in the statistical distribution of hourly precipitation intensities are assessed through the frequency of wet hours, the mean precipitation intensity of wet hours, and the Gini coefficient of hourly precipitation intensities. The Gini coefficient is a nonparametric measure of the concentration of a summable quantity within a population; it is used here to characterize the shape of the distribution of precipitation intensities and quantify the relative contribution of high-intensity extremes. Regarding the space–time dynamics and morphology of storms, we rely on temporal spectral analysis of the hourly precipitation time series and spatial spectral analysis of the hourly precipitation fields. To quantify the uneven change in precipitation variability across spatiotemporal scales, we compute the ratios of future/historical spectral power as functions of the temporal Fourier frequency (period) and of the spatial Fourier wavenumber (wavelength). Additionally, we introduce two summary indicators derived from the Fourier spatial and temporal power spectra: the half-power period (HPP) and the half-power wavelength (HPW), which are measures of the characteristic temporal and spatial scales of precipitation features and patterns.

The analyzed data consist of the outputs of constrained long-term numerical weather simulations with the Weather Research and Forecasting (WRF) Model. Future simulations for the 2041–80 period performed following a pseudo–global warming (PGW) approach (Lucas-Picher et al. 2021; Brogli et al. 2023) are compared to the historical simulation covering the 1981–2020 period. The data are described in detail in section 2. Section 3 presents the methodology and metrics used to quantify change in the spatial and temporal patterns of precipitation across scales (from daily to hourly temporal scales and across mesoscale and submeso-spatial scales). Section 4 presents the results of the comparison of precipitation statistics between the historical and PGW simulations; it is followed by a short analysis of the scale dependence of the results (section 5) and by a summary and discussion (section 6).

## 2. Data: Historical and PGW future WRF simulations

Hourly surface precipitation fields simulated by the WRF Model version 3.8 (Skamarock et al. 2008) at 6-km resolution over the western United States, southwestern Canada, and part of the northeastern Pacific Ocean are analyzed in the present study. The WRF Model was set to simulate atmospheric processes across 35 altitude levels from the surface to the 100-hPa level, with cloud microphysics resolved through the Morrison double-moment scheme (Morrison et al. 2009). For the 1981–2020 historical period, the model is run with lateral boundary conditions and sea surface temperature from the North American Regional Reanalysis (NARR). The PGW simulations are obtained by rerunning the same model, for the same period, with modified NARR boundary conditions. Specifically, the NARR boundary conditions (temperature, water vapor, pressure, and surface variables) are adjusted by adding a perturbation $\Delta$. The perturbation $\Delta$ is specific to each variable and each calendar month and is derived from the difference in the monthly mean values of the corresponding variables between the targeted future period and the historical period in global climate model (GCM) simulations. Three different PGW simulations for the 2041–80 period, with $\Delta$ values from three different CMIP5 GCMs, CESM1-CAM5, CanESM2, and HadGEM2-ES, have been analyzed. The computational cost of the historical simulation and of each one of the PGW simulations is two million CPU hours. The three selected GCMs were retained for their faithful representation of atmospheric rivers in western North America over the historical period (Gao et al. 2015). For all three GCMs, the high-greenhouse-gas-emission scenario, representative concentration pathway (RCP) 8.5 was selected. For conciseness, only the results corresponding to the simulation with perturbation from the CESM1-CAM5 GCM are presented in detail in the present article. Summarized results for the PGW simulations with the other two GCMs (CanESM5 and HadGEM2) are provided in section 4e.

These historical and PGW simulations have been previously utilized in several published studies (Chen et al. 2018, 2019, 2023; Koszuta et al. 2024). More details about the simulation setup are provided in the supplemental material to Chen et al. (2018). Details about the perturbation of the boundary conditions for the PGW simulations are given in the "method" section of Chen et al. (2023). Evaluations of the historical simulation against observations are also reported in these precedent studies; for example, in Chen et al. (2018), comparison with the PRISM dataset (Daly et al. 2008) showed correlation coefficients higher than 0.9 between the WRF historical simulation and PRISM in terms of daily precipitation amounts across 1080 watersheds located within the simulation domain. Further evaluation of the historical simulation is provided as supplemental material to the present article (Fig. S1 in the online supplemental material), showing that, for three of the specific aspects and metrics we focus on in the present study, namely, frequency of wet hours, mean hourly precipitation intensity, and temporal concentration of the precipitation volume measured through the Gini coefficient, the cold-season spatial climatic patterns of the historical simulation are highly

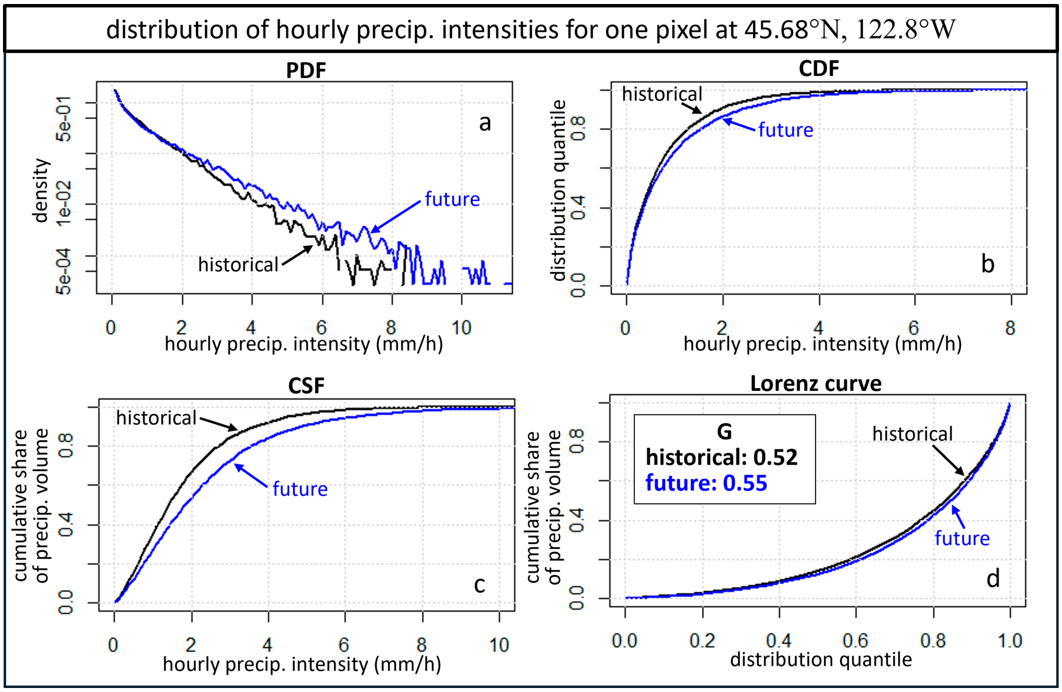


FIG. 1. Historical and future distributions of cold-season hourly precipitation intensities (excluding zeros) for an arbitrarily selected pixel of the simulation domain at coordinates 45.68°N, 122.8°W, near Portland, Oregon. The distributions are shown as empirical (a) PDF, (b) CDF, (c) CSF, and (d) Lorenz curve. From the Lorenz curve, we compute the Gini coefficient as $G = 1 - 2\Gamma$, where $\Gamma$ is the area under the Lorenz curve.

consistent with those of the CONUS 404 high-resolution regional hydroclimate reanalysis (Rasmussen et al. 2023).

## 3. Methodology and metrics

### a. Distributions of precipitation intensities and Gini coefficient

Classically, the statistical distribution of precipitation intensities is represented through a probability density function (PDF), and various parameters (e.g., empirical moments, shape parameters, etc.) are derived to characterize specific aspects of the PDF. If $f_X$ is the PDF of a variable $X$ (e.g., hourly precipitation intensity at a given location), its cumulative density function (CDF) $F_X$ is defined as

$$F_X(x) = \int_{-\infty}^{x} f_X(u)du. \tag{1}$$

Because we are interested in quantifying the relative contribution of precipitating hours with a certain intensity to the seasonal precipitation accumulation, we also consider the cumulative share function (CSF) of precipitation intensities, defined as

$$\Phi_X(x) = \frac{1}{\overline{X}}\int_{0}^{x} uf_X(u)du, \tag{2}$$

where $\overline{X}$ is the statistical mean of $X$. The value $\Phi_X(x)$ of the CSF at intensity $x$ corresponds to the fractional contribution of hourly intensities between 0 and $x$ to the total precipitation volume. The CSF can be used to describe the distribution of any nonnegative quantity and makes particular sense when this quantity can be "accumulated," as is the case for precipitation intensities, which, if integrated over a certain time period and a certain area, amount to a precipitation volume. While the PDF, CDF, and CSF are uniquely related to each other, considering that the distribution of hourly precipitation intensities at kilometric resolutions is skewed and heavy tailed, and because of the importance of high precipitation extremes in terms of hydrological impacts, the CSF, which puts more emphasis on the higher precipitation intensities, is arguably a more insightful representation than the PDF and CDF in our case. While the CSF has been designated under different names (e.g., "weighted CDF"), and its definition has not been exactly formalized and standardized, the concept has been used several times in precipitation studies (Lebsock and L'Ecuyer 2011; Venugopal and Wallace 2016; Guilloteau et al. 2023). The PDF, CDF, and CSF of hourly precipitation intensities (for wet hours only, i.e., excluding zeros) during the cold season in an arbitrarily selected pixel of the simulation domain (at coordinates 45.68°N, 122.8°W, near Portland, Oregon) are shown in Fig. 1 for both the historical and PGW simulations, as an illustrative example.

The function relating the CSF of $X$ to the CDF of $X$ is the Lorenz curve $L_X$ (Fig. 1d), defined such that

$$L_X[F_X(x)] = \Phi_X(x). \tag{3}$$

The Lorenz curve is often used in economics to represent the distribution of wealth among a population (Gastwirth 1972).

If $X$ is nonnegative, the Lorenz curve is a function from [0, 1] to [0, 1] and, $\forall\, u$ in [0, 1], $L_X(u) \le u$. Interestingly, the Lorenz curve $L_X$ remains unchanged if $X$ is multiplied by a constant positive scaling factor, which means that if $Y = \alpha X$, with $\alpha \in \mathbb{R}^+$, then $L_Y(u) = L_X(u)$. Therefore, changes in the Lorenz curve really characterize changes in the shape of the distribution rather than a linear intensification (or decrease) of all precipitation intensities. Let us consider the quantity:

$$\Gamma_X = \int_0^1 L_X(u)du. \tag{4}$$

Since $0 \le L_X(u) \le u$, it follows that $0 \le \Gamma_X \le 0.5$. If $X$ is constant over time, then $\Phi_X(x) = F_X(x)$, $L_X(u) = u$, and $\Gamma_X = \int_0^1 u du = 0.5$. Classically, the Gini coefficient $G_X$ associated with the distribution $f_X$ and the Lorenz curve $\Phi_X$ is defined as (Gastwirth 1972)

$$G_X = 1 - 2\Gamma_X. \tag{5}$$

By definition, $0 \le G_X \le 1$. Along with the Lorenz curve, the Gini coefficient is often used in economics to measure the concentration of wealth within a population.

Here, we use the Gini coefficient to characterize the shape of the distribution of precipitation intensities during wet hours. In our case, a high Gini coefficient corresponds to a high concentration of the precipitation volume within the wet hours, meaning that a small fraction of the wet hours contributes to a disproportionally high fraction of the precipitation volume. Conversely, a low Gini coefficient corresponds to a low concentration over time, the lower limit being 0, when the precipitation intensity is constant, and all wet hours contribute equally to the precipitation volume. In precipitation studies, the Gini coefficient is sometimes used as an alternative to the coefficient of variation or other measures of concentration relying on parametric representations of the statistical distribution of precipitation intensities (Alijani et al. 2008; Rajah et al. 2014; Monjo and Martin-Vide 2016; Sangüesa et al. 2018; Dong et al. 2021).

### b. Fourier temporal and spatial power spectra, HPP, and HPW

The temporal dynamics of hourly precipitation time series (hyetographs) is evaluated through the temporal Fourier power spectrum in the present study. The power spectrum of the 40-yr hourly precipitation time series is computed in every 6-km-resolution pixel of the simulation domain. The Fourier power spectra do not necessarily show peaks at particular frequencies (the diurnal cycle of precipitation has a low amplitude during the cold season over the simulation domain), yet the general shape of the power spectrum and the decrease rate of spectral power with increasing frequency provide useful information about the temporal dynamics of precipitation.

From the temporal Fourier power spectrum $P(f)$, we define the half-power frequency as the Fourier frequency $f_{\mathrm{hp}}$ such as

$$\int_{f=0}^{f=f_{\mathrm{hp}}} P(f)df = \int_{f=f_{\mathrm{hp}}}^{f=f_s/2} P(f)df, \tag{6}$$

where $f_s$ is the data sampling frequency. This means that 50% of the signal's energy comes from its variations at frequencies lower than $f_{\mathrm{hp}}$ and 50% comes from its variations at frequencies higher than $f_{\mathrm{hp}}$. Interpreting the Fourier power spectrum as the statistical distribution of the signal's energy across frequencies, $f_{\mathrm{hp}}$ is in fact the median frequency of this distribution. The HPP is the inverse of the half-power frequency. The HPP, expressed in time units (minutes, hours, or days), can be interpreted as a characteristic duration of the features/patterns in the precipitation time series (computed as an average over numerous features with potentially very different durations). Small values of HPP correspond to precipitation intensities varying rapidly over short periods of time (sharp hyetographs), and larger HPP values characterize smoother temporal dynamics.

The temporal Fourier spectral analysis of the hourly precipitation time series is complemented by a spatial Fourier spectral analysis of the hourly precipitation fields relying on a two-dimensional Fourier transform. The 2D Fourier spectra are defined as functions of the spatial wavenumber and of the spatial direction (azimuth). In this study, the 2D Fourier spectra are reduced to univariate functions by integration across all azimuths; we thus obtain omnidirectional spatial power spectra which are functions of the wavenumber only. The same way, the half-power frequency is defined as the median frequency of the distribution of spectral energy given by the temporal Fourier power spectrum [Eq. (6)], we define the half-power wavenumber as the median wavenumber of the distribution of spectral energy given by the spatial Fourier power spectrum $P(w)$:

$$\int_{w=0}^{w=w_{\mathrm{hp}}} P(w)dw = \int_{w=w_{\mathrm{hp}}}^{w=w_s/2} P(w)dw, \tag{7}$$

where $w_s$ is the data spatial sampling wavenumber (the number of samples per distance unit, i.e., the inverse of the grid spacing interval for spatially gridded data). The HPW expressed in distance units (km in the present study) is the inverse of the half-power wavenumber. The HPW derived from the spatial Fourier power spectrum can be interpreted similarly to the correlation distance derived from the spatial correlogram or variogram but has the advantage of not relying on a parametric representation of the structure function (power spectrum variogram or correlogram). Small values of the HPW correspond to precipitation fields showing large magnitudes of precipitation gradients over short distances; conversely, large HPW values correspond to precipitation fields showing high correlation between precipitation intensities in nearby locations (i.e., smoother spatial fields with larger characteristic length scales).

## 4. Results

In this section, we present in detail the statistical comparison of the outputs of the 2041–80 PGW simulation with perturbation of the boundary conditions derived from the CESM1-CAM5 model, RCP8.5 scenario, to that of the 1981–2020 historical simulation. The analysis focuses exclusively on the October–March

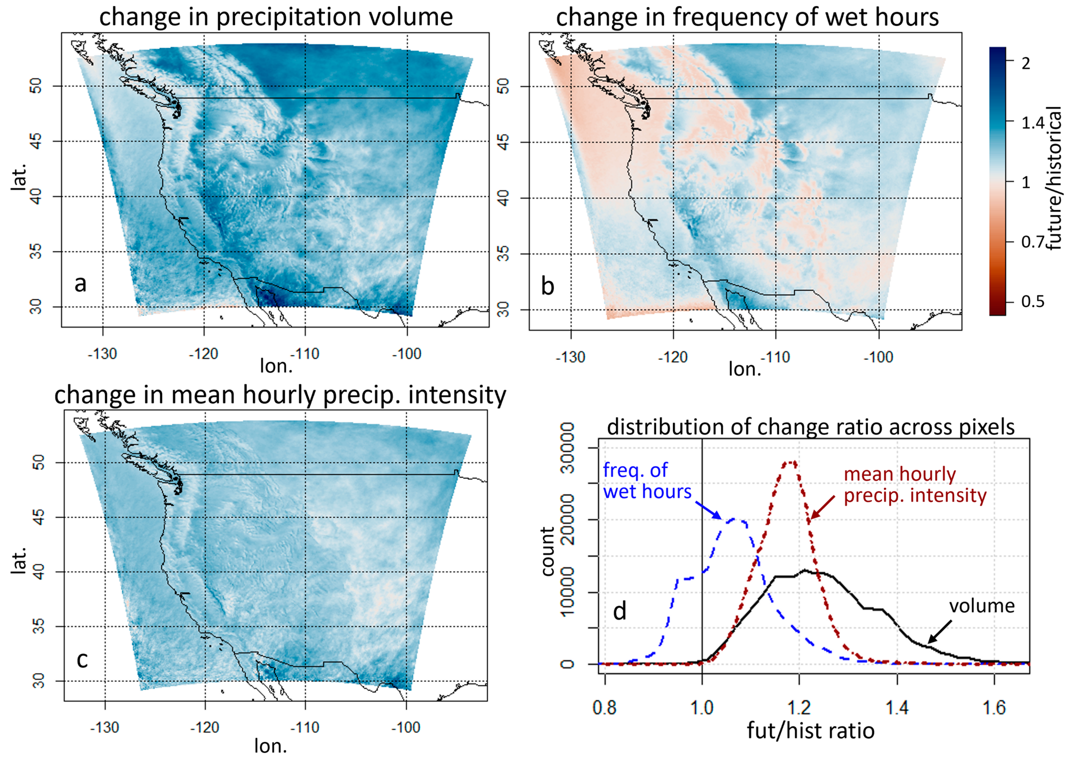


FIG. 2. Change in (a) cold-season precipitation volume, (b) frequency of wet hours, and (c) mean hourly precipitation intensity, between the historical simulation (1981–2020) and the CESM1-CAM5 PGW simulation (2041–80). The frequency of wet hours is computed as the fraction of all hours with precipitation intensity above zero. The mean hourly precipitation intensity is computed as the mean intensity of all wet hours (i.e., excluding zero-intensity hours). For each statistic, the change is expressed as the ratio of the future value over the historical value (change ratio). The statistical distributions of change ratios across the pixels of the simulation domain for all three statistics are shown in (d).

cold season which concentrates most of the annual precipitation volume in western North America.

### *a. Precipitation volume, frequency of wet hours, and mean hourly intensity*

We first focus on the change in the mean cold-season precipitation volume, which we decompose as the number of wet hours (hours with nonzero precipitation) multiplied by the mean hourly precipitation intensity (the mean intensity of all wet hours), at the 6-km pixel resolution. The cold-season precipitation volume is found to increase nearly everywhere within the simulation domain from the historical simulation to the PGW simulation, as 98% of the pixels see a 4% or more increase (Fig. 2). The increase rate of the average precipitation volume within the simulation domain is +18%, and the median value of the per-pixel distribution of relative change in precipitation volume is +24%. Noticeably, a proportionally larger increase in the precipitation volume occurs on the leeward side (eastern slopes) of the Cascades and Sierra Nevada mountain ranges as compared to the windward side (western slopes), as reported in Huang et al. (2020) and Koszuta et al. (2024).

Regarding the frequency of wet hours, the changes between the historical simulation and the PGW simulation are more spatially contrasted: While a majority of pixels, 60%, see a +4% or more increase in wet-hour frequency, 12% of pixels see a decrease of at least −4%. The areas where the wet-hour frequency decreases are essentially the Pacific Ocean above 40°N, the coastal areas of the Pacific Northwest, and parts of the Rocky Mountains (Fig. 2b). While 50% of the pixels show relative increase in the frequency of wet hours of +6% or more, the average frequency of wet hours within the simulation domain only increases by +2.8% (as areas with increasing frequency of wet hours and areas with decreasing frequency of wet hours tend to cancel out in average). The mean hourly precipitation intensity (mean intensity of wet hours) is found to increase nearly everywhere within the simulation domain as 99% of pixels see a +4% or more increase. The median per-pixel increase is +17%, and the increase in the mean hourly intensity averaged over all pixels is +14.5%. The increase in the mean hourly intensity is remarkably homogeneous across space (Fig. 2c) as compared to the change in the frequency of wet hours. The spatially homogeneous increase in the precipitation intensity drives the increase in the spatially averaged cold-season precipitation volume over the simulation domain. On the leeward side of mountains, the conjoint increase in precipitation intensity and wet-hour frequency produces larger increase in the precipitation volume than on the windward side, where the increase in intensity is partially counterbalanced by the decrease in wet-hour frequency.

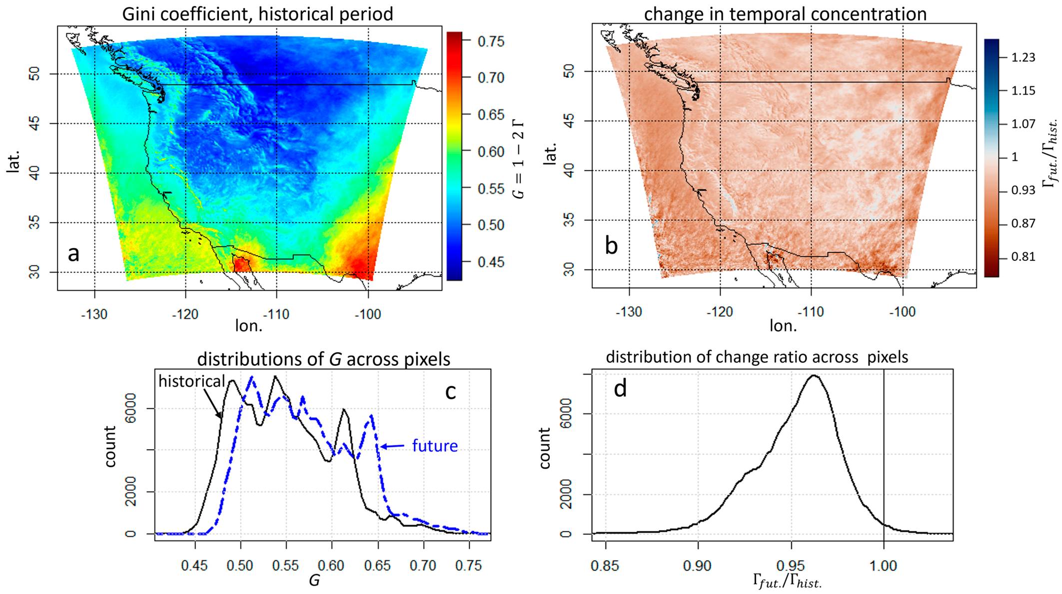


FIG. 3. Change in the temporal concentration of the precipitation volume across wet hours during the cold season between the historical simulation (1981–2020) and the PGW simulation (2041–80). (a) Map of the Gini coefficient $G = 1 - 2\Gamma$ of the temporal distribution of intensities for the historical simulation. (b) Map of the change ratio $\Gamma_{futur}/\Gamma_{historical}$ per pixel. (c) Distribution of the Gini coefficient across all pixels, for the historical and PGW simulations. (d) Statistical distribution of the change ratio $\Gamma_{futur}/\Gamma_{historical}$ across all pixels.

Considering that the temporal statistics are computed over 40-yr-long hourly time series (i.e., about 175 000 samples excluding the warm season), a proportional change of ±2% in the frequency of wet hours or mean precipitation intensity is statistically significant at the $10^{-4}$ level.

### b. *Distribution of hourly precipitation intensities, temporal concentration, and Gini coefficient*

We now focus on the full statistical distribution of hourly precipitation intensities during the wet hours at each pixel, instead of their mean value only. We use the Gini coefficient to assess changes in the shape of the distribution of nonzero precipitation intensities. This measure of change in the shape of the distribution is agnostic to linear scaling between historical and future precipitation intensities, the linear scaling having already been quantified through the ratio of future mean intensity over historical mean intensity (Fig. 2c). The Gini coefficient, being a bounded quantity computed through first-order integrals, is stable and resilient to outliers (unlike most of other statistical shape parameters, which generally relate to the second- and higher-order moments of the distribution). Figure 3a shows the value of the Gini coefficient of the temporal distributions of cold-season hourly precipitation intensity, computed in each pixel of the simulation domain, for the historical period. Figure 3c shows the future and historical distributions of the Gini coefficient $G$ across all the pixels. One can see that the distribution of the Gini coefficient is shifted toward higher values in the future as compared to the historical simulation. Figs. 3b,d show the relative change in the temporal concentration of precipitation intensities across every pixel. Because the historical Gini coefficient is higher than 0.5 in most pixels, we quantify the change in the concentration through the ratio $\Gamma_{future}/\Gamma_{historical}$ rather than the ratio of the future and historical Gini coefficients [with $\Gamma = 0.5 \times (1 - G)$ from Eq. (5)]. This allows to better highlight change in pixels where the historical value of $G$ is high (i.e., with low value of $\Gamma_{historical}$). The $\Gamma$ coefficient is found to decrease in 99% of the pixels, meaning that the Gini coefficient measuring the concentration of the precipitation volume within the wet hours increases in 99% of the pixels. Similarly to the mean precipitation intensity (Fig. 1c), the increase in the temporal concentration of precipitation is remarkably homogeneous across the simulation domain (Fig. 3b). The increase in the Gini coefficient reflects the fact that the intensity of the higher quantiles of the distributions increases proportionally more than that of the lower quantiles from the historical simulation to the future simulation. This finding is consistent with numerous studies that suggest that high precipitation extremes increase (or will increase) at a higher rate than low and medium intensities under global warming (Papalexiou and Montanari 2019; Kunkel et al. 2020; Thackeray et al. 2022).

### c. *Temporal and spatial power spectra, half-power period, and half-power wavelength*

We now focus our analysis on the temporal dynamics of hourly precipitation, to try to understand how changes in the statistical distribution of intensities relate to changes in the form of the hyetographs. This part of the analysis relies on the comparison of the Fourier power spectra of the hourly precipitation time series during the cold season for the future simulation with that of the historical simulation. Figure 4a shows the Fourier power spectra of the winter precipitation

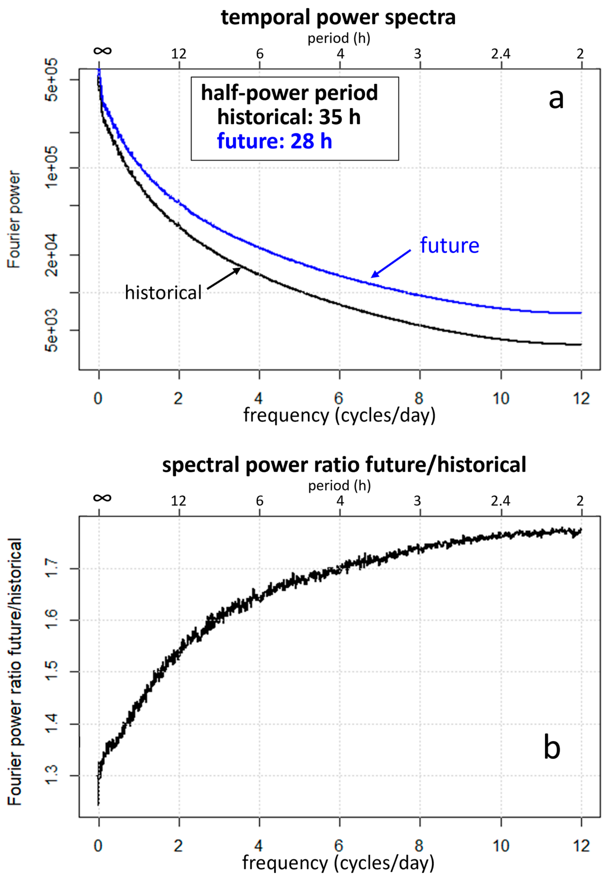


FIG. 4. Change in the Fourier power spectrum of the winter precipitation time series. (a) Historical and future power spectra. The power spectra are computed using a fast Fourier transform in each pixel and for each year's cold season (October–March) and then averaged over all pixels and all 40 years. From the Fourier power spectrum $P(f)$, we determine the half-power frequency $f_{\mathrm{hp}}$ such as $\int_{f=0}^{f=f_{\mathrm{hp}}} P(f)df = \int_{f=f_{\mathrm{hp}}}^{f=f_s/2} P(f)df$, where $f_s$ is the sampling frequency (24 cycles day$^{-1}$ in our case). The HPP is the inverse of the half-power frequency. (b) Ratio of the future spectral power over the historical spectral power as a function of the Fourier frequency.

time series, averaged over all pixels and all 40 years (the power spectra at each pixel are averaged together, not the time series). One can see that the spectral power is systematically higher in the future as compared to the historical period, which corresponds to an increase in the statistical variance of hourly precipitation intensity time series [the statistical variance equals the integral of the spectral power over $(0, f_s/2]$, where $f_s$ is the sampling frequency]. The increase is proportionally higher at higher frequencies (Fig. 4b), which indicates that the magnitude of short-duration features increases proportionally more than that of longer-duration features. The power spectrum is "whitening" in the future: As the decrease rate of the spectral power with frequency dampens, the power spectrum gets more similar to that of a white noise. This reveals that the propensity of precipitation intensity to vary (increase or decrease) rapidly over short periods of time is enhanced in the future. We can describe this change as a "sharpening" of the hyetographs. Fig. S2 illustrates with idealized synthetic data how changes in the shape of the hyetographs generally translate in terms of change in the Fourier power spectrum.

In the following, we use the HPP as a measure of the "sharpness" of the hyetographs. Shorter HPPs correspond to sharper hyetographs, and longer HPPs correspond to smoother hyetographs. The HPPs computed from the pixel-averaged Fourier power spectra (Fig. 4a) for the historical and PGW simulations are, respectively, 35 and 28 h. Figure 5 shows the change in the HPP across the different pixels of the study domain. The HPP decreases in 77% of the pixels. One shall note that the Fourier power spectrum of the intensity time series is affected by the zeros, and therefore, so is the HPP. Generally, higher fraction of zeros (lower frequency of wet hours) and shorter storm durations correspond to lower HPP. For the historical period, for example, the pixel values of the frequency of wet hours and of the HPP are positively correlated (CC = 0.82). However, even though a majority of pixels (76%) see an increase in the frequency of wet hours, a majority of pixels (77%) see a decrease of the HPP. This means that, in many pixels, the effect of the sharpening of the hyetograph during the wet periods on the Fourier power spectrum dominates the effect of the increasing number of wet hours. The pixels for which the HPP is not decreasing are essentially located in the Canadian part of the Northern Prairie, where the frequency of wet hours increases by more than 20% (see Fig. 1b). This dramatic increase in the frequency of wet hours in the Northern Prairie can be explained by increased amount of water vapor in atmospheric rivers and water vapor being transported further inland during atmospheric river events. Atmospheric rivers that were only affecting the westernmost regions of the simulation domain in the historical simulation penetrate further inland and reach the Northern Prairie more frequently in the PGW simulation. While the sharpening is also occurring in the Northern Prairie, the increase in the frequency of wet hours dominates the statistics of change in this region.

We now assess how changes in the temporal dynamics of precipitation relate to changes in the morphology of storms and the spatial patterns in hourly precipitation fields through spatial Fourier analysis. For each hour, in both the historical simulation and the PGW, the omnidirectional spatial Fourier power spectrum of the precipitation intensity map over the simulation domain is computed. All hourly power spectra between October and March are then averaged over the 40 years of the simulation. Similarly to what is seen in the temporal power spectrum (Fig. 4), an increase in the spectral power at all spatial wavenumbers is observed in the spatial power spectrum (Fig. 6), reflecting the increase in the spatial variance of the precipitation fields. Consistently with what was shown by the temporal power spectra, for the spatial spectrum, the spectral power increases proportionally more at higher wavenumbers, reflecting a spatial sharpening of the precipitation features, meaning that the spatial variability (spatial gradients) associated with small-scale features increases more significantly than that of the larger-scale features. Specifically, the spectral power associated with large

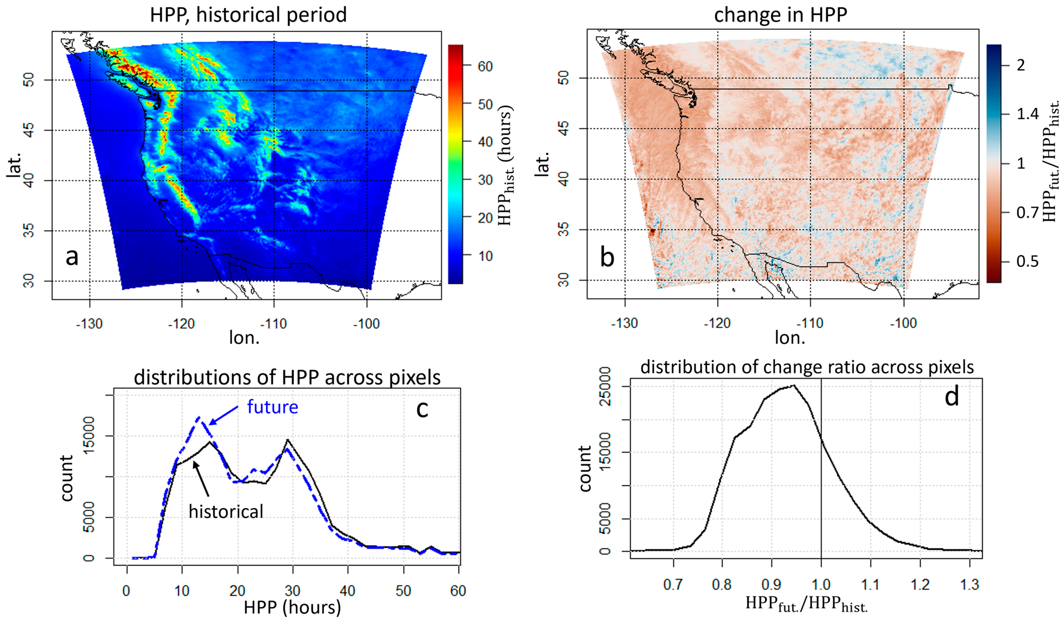


FIG. 5. Change in the HPP of hourly precipitation time series during the cold season between the historical simulation (1981–2020) and the PGW simulation (2041–80). (a) Map of the HPP for the historical simulation. (b) Map of the change ratio $HPP_{future}/HPP_{historical}$ per pixel. (c) Distribution of the HPP across all pixels for the historical and PGW simulations. (d) Statistical distribution of the change ratio $HPP_{future}/HPP_{historical}$ across all pixels.

scales (wavelength > 200 km, i.e., meso-alpha and synoptic scales) increases by 35%–45%, the spectral power associated with the meso-beta scale (200 km > wavelength > 20 km) increases by 45%–75%, and the spectral power associated with the submesoscales (wavelength < 20 km) increases by 75%–90%. One must note that the 6-km resolution of the simulations only allows to resolve wavelengths coarser than 12 km. The spectral analysis shows that the amplification of precipitation variability in the PGW simulation as compared to the historical simulation becomes increasingly salient when analyzing increasingly fine temporal and spatial scales. This suggests that simulations with resolutions even finer than those analyzed in the present study may therefore be necessary to fully apprehend the changing nature of precipitation under global warming.

The HPW, which is the spatial equivalent of the half-power period, is reduced from 385 to 278 km from the historical simulation to the PGW simulation (Fig. 6). Figure 7 shows the local change in HPW across the different pixels of the domain. To allow the computation of spatially localized power spectra, a continuous 2D wavelet transform relying on the isotropic Ricker wavelet (Mexican hat wavelet) is used (Antoine et al. 1993). The continuous wavelet transform provides the same information as the Fourier transform, with the advantage of being localized. As previously with the Fourier spatial transform, the continuous spatial wavelet transform is applied on each hourly precipitation map between October and March and the spectra are averaged over 40 years. Even if a fairly high variability in the change ratio from one pixel to the next can be observed over land, the general pattern shows the HPW decreasing in most pixels (79% of the pixels). The decrease is particularly salient over the Pacific Ocean above the 37°N latitude. The more complex patterns and higher variability over land can be attributed to the local effect of orography on storms' morphology.

### *d. Gini coefficient of the spatial distribution of precipitation*

In this last result section, we assess how the change in precipitation under global warming manifests itself in terms of the spatial concentration of the precipitation volume. Here again, we rely on the Gini coefficient as a measure of concentration. However, instead of assessing the temporal concentration at a given location (pixel), we assess the spatial concentration at a given time, by looking at the distribution of intensities across pixels. Figure 8 shows the Lorenz curve of the distribution of the mean cold-season precipitation volume across all the pixels of the simulation domain, for the historical and PGW simulations. In terms of the spatial distribution of the mean seasonal precipitation volume, the Gini coefficient decreases from 0.50 for the historical period to 0.47 in the future (a statistically significant difference at the $10^{-15}$ level according to the Kolmogorov–Smirnov test), meaning a more homogenous spatial distribution in the future. Indeed, the mean seasonal precipitation volume tends to increase proportionally more in semiarid areas such as California, Nevada and Arizona, the Northern Prairie, the Columbia Plateau, the Interior plateau in British Columbia, and the eastern (leeward) slopes of the Sierra and Cascade Mountains, than in wet regions such as the coastal parts of Oregon, Washington, and British Columbia and the western (windward) slopes of the Cascade and Rocky Mountains (see Fig. 2a). This finding

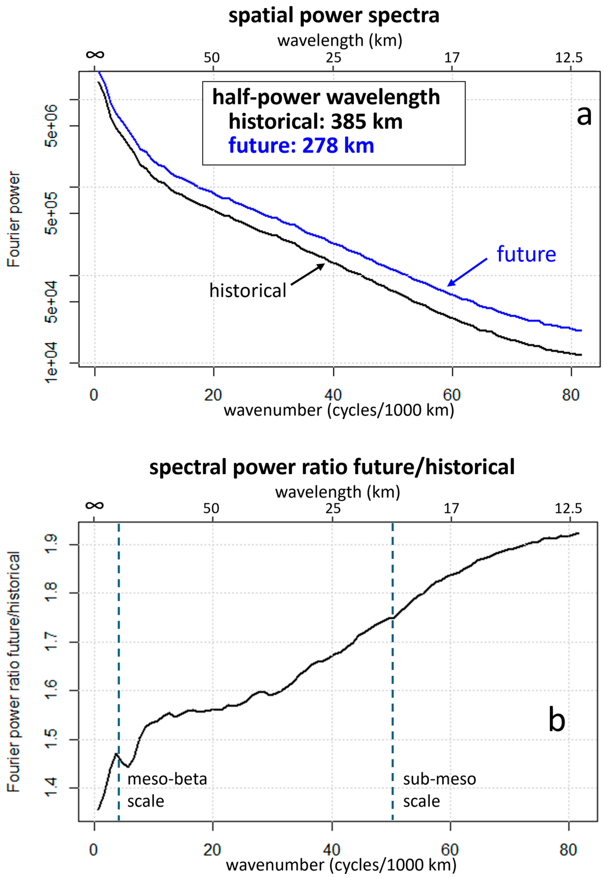


FIG. 6. Change in the spatial Fourier power spectrum of the hourly precipitation fields. (a) Historical and future power spectra. The power spectrum of each hourly precipitation field during the cold season (October–March) is computed using a 2D fast Fourier transform over the whole simulation domain. The hourly power spectra are then averaged over the 40 simulated years.

seems to go against the "wet gets wetter, dry gets dryer" paradigm, often suggested in the literature to describe changing patterns of precipitation under global warming (Chou et al. 2009; Liu and Allan 2013; Polson and Hegerl 2017; Zaitchik et al. 2023). One must however note that, within our simulation domain, the regional and local spatial patterns are essentially driven by orography. The Koszuta et al. (2024) study, derived from the same dataset as the one used for the present analysis, discusses in detail the weakening of the orography-driven patterns; its findings are found to apply to other regional simulations in which orographic effects are resolved. In contrast, the "wet gets wetter, dry gets dryer" paradigm generally refers to the synoptic patterns associated with moisture transport and the projected expansion of the Hadley cell (Lu et al. 2007; Vallis et al. 2015). The "wet gets wetter, dry gets dryer" paradigm is in fact mostly relevant to tropical and subtropical regions, and its general validity is subject to controversy over land in particular (Byrne and O'Gorman 2015).

One must note that the fact that the mean cold-season precipitation volume is more homogeneously distributed across the simulation domain in the future does not mean that precipitation is more homogeneously distributed within individual storms. In fact, the increasing Fourier spectral power at fine scales and the decreasing half-power wavelength (Figs. 6 and 7) suggest the opposite. To locally assess the spatial distribution of hourly precipitation intensities during storms, we define four climatically and geographically homogeneous subregions within the study domain and focus on the 1500 rainiest hours (in terms of regionally averaged precipitation intensity) in each subregion, over 40 years, for both the historical simulation and the PGW simulation. The subregions, defined as the coastal parts of Oregon and Washington (excluding the Olympus Peninsula), the plains of California (coast and Central Valley), the Northern Prairie (east of the Rocky Mountains above 46°N), and the Pacific Ocean between 40° and 50°N, are represented in Figs. 9 and 10 (top panels). For each subregion, and for each one of the 1500 rainiest hours, the Gini coefficient of the spatial distribution of hourly precipitation intensities across all the pixels of the subregion of interest (at 6-km resolution) is computed. The statistical distribution of the 1500 Gini coefficients computed for the PGW simulation is compared to the distribution for the historical period (Figs. 9 and 10, lower panels). One can see that for the Oregon–Washington, California, and Pacific Ocean subregions, the distribution of the Gini coefficients is shifted toward higher values in the future. For the Oregon–Washington subregion, the median value of the Gini coefficient increases from 0.46 to 0.50, over California, it increases from 0.55 to 0.57, and over the Pacific Ocean, it increases from 0.69 to 0.73. In all three regions, the change in the distribution of the Gini coefficients is statistically significant at the 0.001 level according to the Kolmogorov–Smirnov test. Over the Northern Prairie, the historical and future distributions of the Gini coefficients are not significantly different from each other ($p$ value of 0.75). Over the three other regions, the increase in the spectral energy at short wavelengths (Figs. 6 and 7) corresponds to an increased spatial concentration of the hourly precipitation volume. The temporal sharpening of the hyetographs discussed in the previous section thus concurs with a spatial sharpening of the storms. This spatial sharpening is consistent with the findings of the Chen et al. (2023) study, which presents an object-based analysis of storm morphology at the daily resolution from the same dataset as the one used here.

It is worth noting that, when it comes to the spatial concentration and variability of storms, the change is most salient over the Pacific Ocean, above 37°N (Figs. 7 and 10). Over midlatitude oceans, the formation and evolution of precipitation systems is essentially driven by the atmospheric conditions (including temperature and humidity). Over land, precipitation patterns are influenced by a wider range of factors, including orography which can have a strong local influence, rendering the patterns more complex and more variable.

### e. *Multi-GCM PGW simulations*

Repeated analyses with PGW simulations constrained by two other GCMs, CanESM2 and HadGEM2-ES, also under the RCP8.5 scenario, provided consistent results regarding

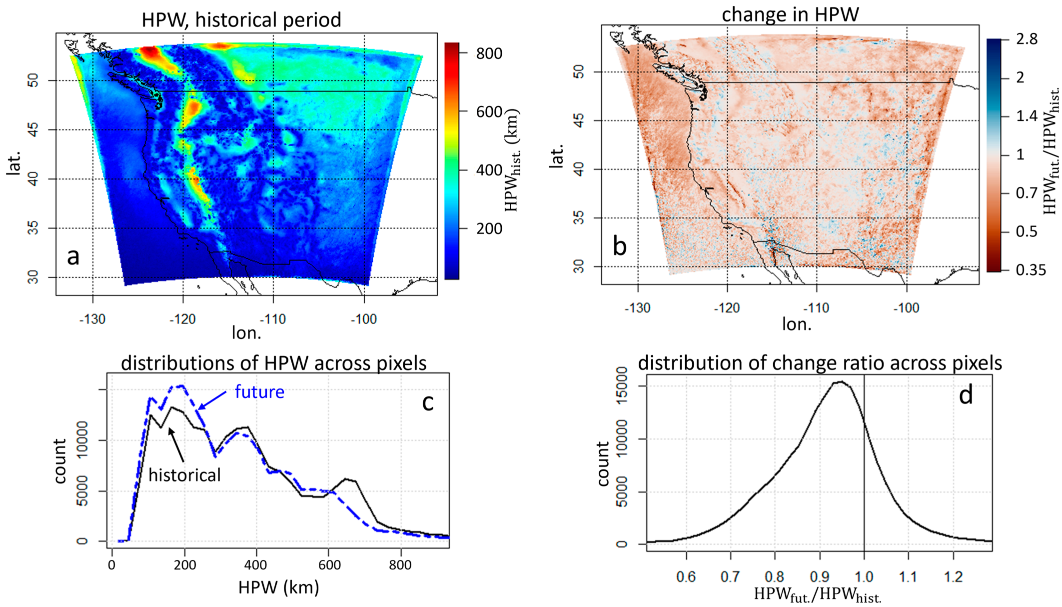


FIG. 7. Change in the HPW of the cold-season hourly precipitation fields between the historical simulation (1981–2020) and the PGW simulation (2041–80). (a) Map of the HPP for the historical simulation. (b) Map of the change ratio $HPW_{future}/HPW_{historical}$ per pixel. (c) Distribution of the HPW across all pixels for the historical and PGW simulations. (d) Statistical distribution of the change ratio $HPW_{future}/HPW_{historical}$ across all pixels.

the increase in the mean precipitation intensity during the wet hours, and the increase in the concentration of the precipitation volume within the wet hours, measured through the Gini coefficient (Fig. 11), as well as the increase in the spectral power at the high temporal frequencies and high spatial wavenumbers (Fig. 12). The change in the frequency of wet hours

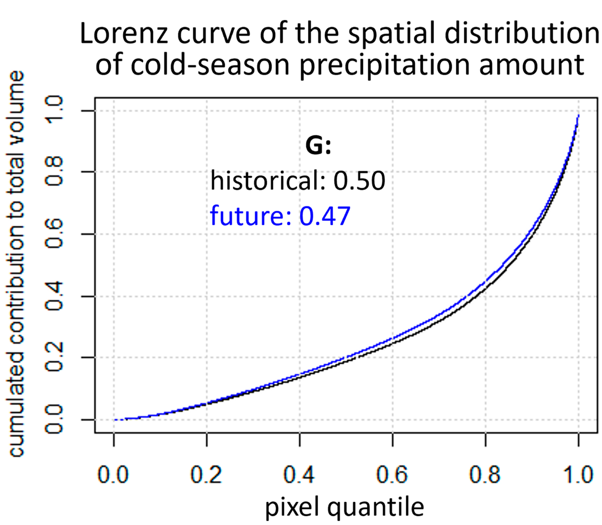


FIG. 8. Lorenz curves of the spatial distributions of the 40-yr-mean cold-season precipitation amount across all the pixels of the simulation domain, at 6-km resolution, for the historical and PGW simulations. The difference between the future and historical Gini coefficients is statistically significant at the $10^{-15}$ level according to the Kolmogorov–Smirnov test.

is more contrasted across simulations, with the HadGEM2-ES simulation in particular showing a decrease in the frequency of wet hours in 60% of the pixels. It is interesting to note that the statistic showing the most spatially contrasted changes, the frequency of wet hours, is also the statistic showing the most contrast across the different PGW simulations. The differences between the three PGW simulations reveal how the uncertainties in the future boundary conditions propagate through the storm-resolving WRF simulation scheme. Taking the variability of the statistics across the different PGW simulations as a measure of uncertainty, it appears that, while future change in the frequency of wet hours within the simulation domain is rather uncertain, the increase in the mean hourly precipitation intensity and in the concentration of the precipitation volume within wet hours are predicted with reasonably high confidence under the assumptions of the PGW simulation setup.

## 5. Scale dependence of the statistics

As mentioned in the introduction, comprehensively assessing change in precipitation is made a difficult and cumbersome task by the scale dependence of the statistical distributions. For example, the results of the previous section show increasing spatial concentration of precipitation at the hourly time scale during the 1500 rainiest hours of the record within most subregions (Figs. 9 and 10) but decreasing spatial concentration across the whole simulation domain of the seasonal precipitation volume (Fig. 8). Spectral analysis, as presented in section 4c, allows to partially assess the signal's variability across multiple scales. However, power spectra fundamentally relate to the autocovariance/autocorrelation of the signal and thus only

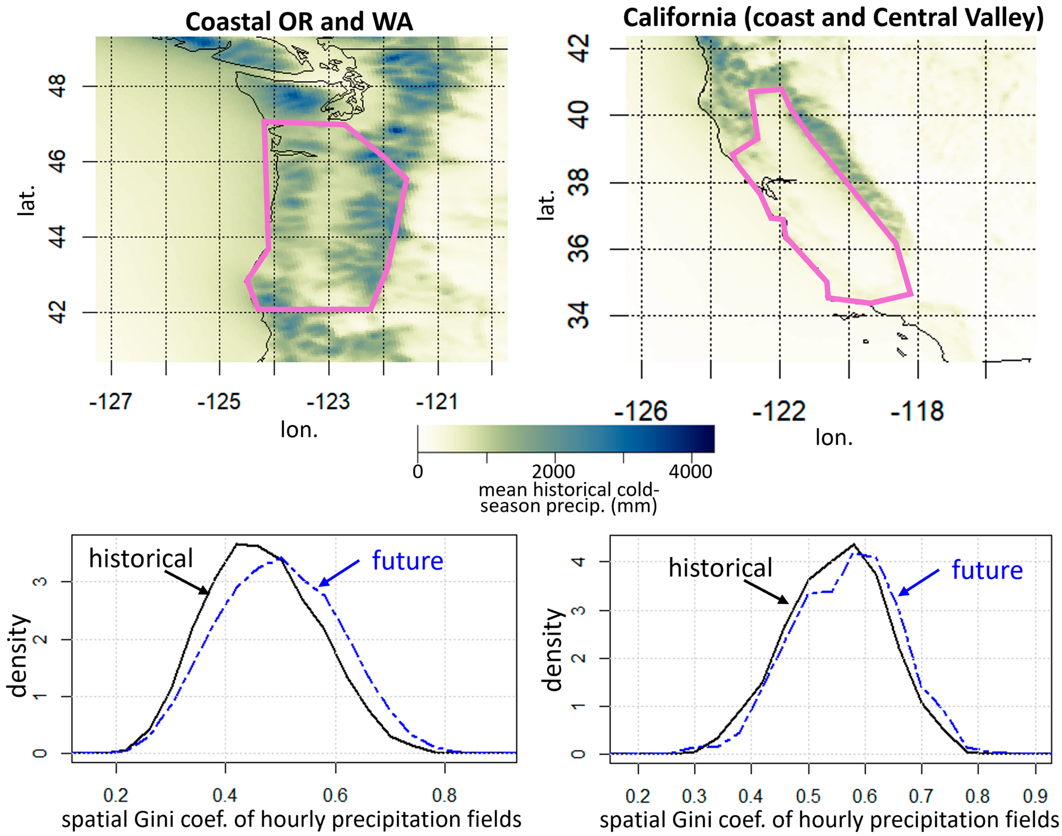


FIG. 9. Statistical distributions of the Gini coefficients characterizing the spatial distributions of hourly precipitation intensities across the pixels of the Oregon–Washington and California subregions of each one of the 1500 rainiest hours in each subregion. The distributions for the PGW simulation (2041–80) are compared to the distributions for the historical simulation (1981–2020).

characterize the dependence of the second statistical moment (variance) to scale/resolution. In our case, the spectral analysis suggested that the finer the scale, the higher the magnitude of the change (in terms of both temporal and spatial scales, Figs. 4 and 6), at least within the range of scales resolved by the simulations. Yet it is important to assess up to which scales the change is appreciable. Figure 13 shows the distribution of the change ratio across the pixels of the simulation domain, for the frequency of occurrence of precipitation (i.e., the frequency of wet hours, frequency of wet days), the mean precipitation intensity during wet periods, and the concentration of the temporal distribution of precipitation intensities during wet periods, when the data are analyzed at 6-km and 24-h resolution and 102-km and 1-h resolution, in addition to the original 6-km and 1-h resolution. The objective here is to assess the sensitivity of the results to both spatial and temporal resolutions.

The frequency of occurrence of precipitation is the statistic for which the change is the most contrasted across different resolutions. At the original 6-km and 1-h resolution, 76% of pixels see an increase in the frequency of occurrence of precipitation and the median change value is +6%. At the 102-km and 1-h resolution, 79% of pixels see an increase in the frequency of occurrence of precipitation and the median change value is also +6%. At the 6-km and 24-h resolution, 92% of pixels see an increase in the frequency of occurrence of precipitation and the median change value is +12%. Regarding the mean precipitation intensity during wet hours (or wet days), the change is more consistent across resolutions, with increasing values in more than 99% of the pixels at all resolutions. The magnitude of the increase is however variable across scales with median values of +17.3%, +15.8%, and +13.4%, respectively, at 6-km and 1-h resolution, 102-km and 1-h resolution, and 6-km and 24-h resolution. Finally, change in the temporal concentration as measured by the Gini coefficient is also showing consistency across resolutions. The $\Gamma$ increases and thus $G$ decreases in more than 96% of the pixels at all resolutions. The median values of the $\Gamma$ decrease rate are fairly similar at different resolutions, with −4.4% at the 6-km and 1-h resolution, −4.0% at the 102-km and 1-h resolution, and −3.9% at the 1-km and 24-h resolution.

To summarize this analysis of the scale dependence of the change in precipitation statistics, increases in the (zero-excluded) mean precipitation intensity and in the Gini coefficient are observed at all three selected resolutions but are most salient at the finest 6-km and 1-h resolution. The frequency of occurrence of above-zero precipitation intensity shows a more complex scale dependence; at the coarser 24-h

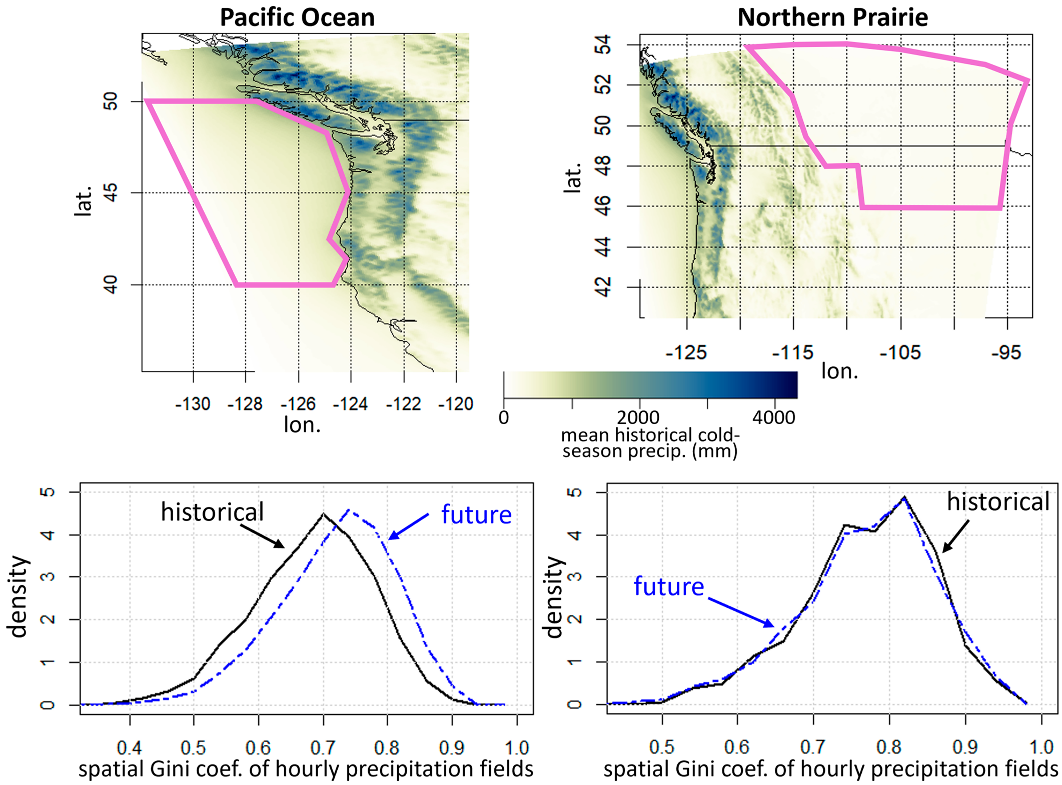


FIG. 10. As in Fig. 9, but for the Pacific Ocean and northern Prairie subregions.

temporal resolution, the frequency of occurrence appears to increase in most pixels and proportionally more than that at the 1-h resolution. While the increase in the precipitation volume is essentially driven by an increase in the mean hourly precipitation intensity within the wet hours, if the data are analyzed at the daily resolution, the statistics show a substantial increase in the wet-day frequency, by 8.5% on average over the simulation domain (against an increase of only 2.8% in the wet-hour frequency), and conversely a lower increase in the mean intensity of above-zero values than at the hourly resolution. This is a clear example of the fact that analyses of the same dataset, with the same methodology, at different resolutions, can lead to seemingly diverging findings and different interpretations.

## 6. Summary and discussion

### a. Summary

Changes in cold-season precipitation statistics between historical and PGW simulations over the western United States and southwestern Canada were analyzed. The comparison of the 2041–80 PGW simulation with perturbations of boundary conditions from the CESM1-CAM5 model under the RCP8.5 scenario to the historical 1981–2020 simulation revealed an increase in the cold-season precipitation volume (+18% in average), mostly driven by an increase in the mean intensity of wet hours (+14.5% in average), across the whole simulation domain. The frequency of wet hours showed more contrasted changes within the domain with a general increase (+2.8% in average) but also a decrease in a significant fraction of the simulation domain, essentially over the Pacific Ocean above 40°N, the coastal areas of the Pacific Northwest, and parts of the Rocky Mountains.

Our analysis also assessed the change in the temporal concentration of precipitation during the wet hours through the Gini coefficient. The Gini coefficient of the distribution of precipitation intensities was found to increase in 99% of the pixels, meaning that the proportional contribution of the high-intensity wet hours to the total precipitation volume increases in the future: The intensity values associated with the higher quantiles of the distribution increase at a higher rate than the mean of the distribution. This sharpening of the hyetographs at the hourly resolution is accompanied by an increase of the statistical variance. The spectral analysis revealed that the additional variability (variance/energy) is essentially carried by the fine subdaily temporal scales, as the spectral power increases proportionally more at higher Fourier frequencies. The statistical consequence of this is a decrease of the half-power period (HPP) in 77% of the pixels.

The analysis of the temporal variability was complemented by an analysis of the spatial variability. The half-power wavelength (HPW), which is the spatial equivalent of the HPP, computed from the spatial power spectra of hourly precipitation intensity fields, decreases over 79% of the pixels of the domain. The spatial spectral power is found to increase more significantly at shorter spatial wavelengths, with a 45%–75%

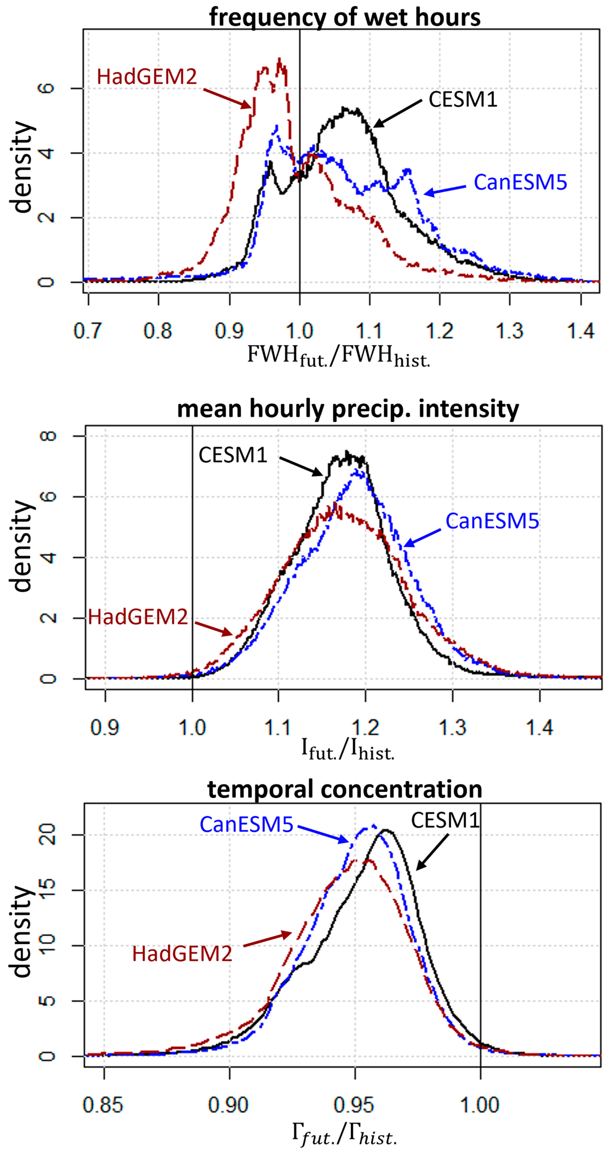


FIG. 11. Statistical distributions of the change ratio (ratio of the future value over the historical value) across all the pixels of the simulation domain, for the frequency of wet hours, the mean precipitation intensity of wet hours, and the coefficient Γ derived from the Lorenz curve, for three different pseudofuture simulations constrained by three different GCMs. The three GCMs are CESM1-CAM5, CanESM2, and HadGEM2-ES.

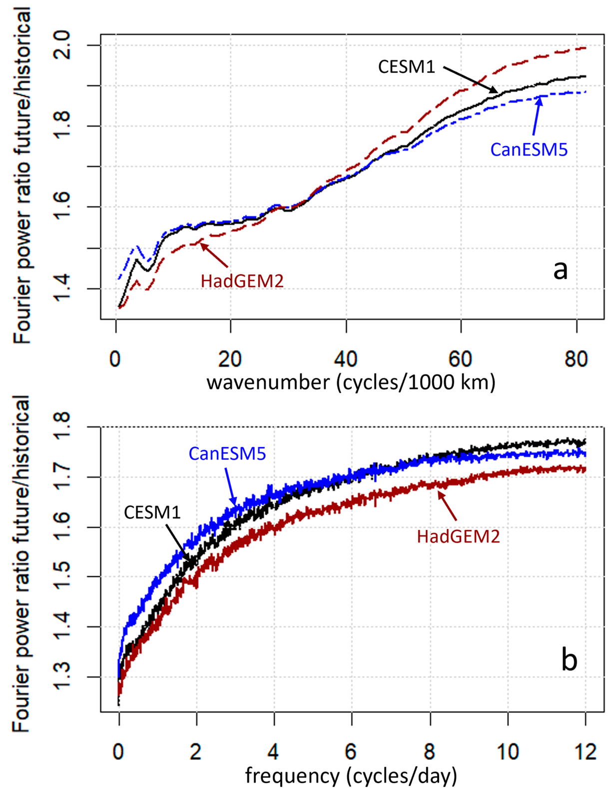


FIG. 12. (a) Ratio of the future spectral power over the historical spectral power as a function of the Fourier spatial wavenumber for three different pseudofuture simulations constrained by three different GCMs. (b) Ratio of the future spectral power over the historical spectral power as a function of the Fourier temporal frequency for three different pseudofuture simulations constrained by three different GCMs. The three GCMs are CESM1-CAM5, CanESM2, and HadGEM2-ES.

increase at the meso-beta scale (200 km > wavelength > 20 km) and up to 90% increase at the submesoscale (wavelength < 20 km). Similarly to what is found regarding the temporal structure of the hyetographs, the increase in the spectral power at fine scales in the spatial spectra corresponds to a sharpening of the smaller spatial features in hourly precipitation fields. Over the Pacific Ocean, along the coastal regions of Oregon and Washington, and in the plains of California, the statistical distribution of the Gini coefficients characterizing the spatial distributions of hourly precipitation intensities within the 1500 most intense rainy hours over 40 years is shifted toward higher values in the PGW simulation. This means that, at the hourly time scale, the precipitation volume becomes more concentrated inside a smaller fraction of the storm area, where the most intense precipitation occurs.

### b. Discussion

The statistical analysis presented here relies exclusively on direct empirical statistics, without parametric fitting, preprocessing of the data, object extraction, thresholding, or quantile selection. It is therefore relatively straightforward to reproduce and apply across multiple large datasets. The computational complexity of all the algorithms used here is of order $N$, where $N$ is the size of the data. This matters as, in our specific case for example, even if we considered one variable only, and only one altitude level (surface level), for each simulation (PGW or historical), the output data are made of $3.4 \times 10^{10}$ samples (193 600 pixels times 4380 h times 40 years).

The change in the temporal and spatial structure was assessed through spectral analysis among other statistics. While power spectra may be challenging to apprehend for nonexperts

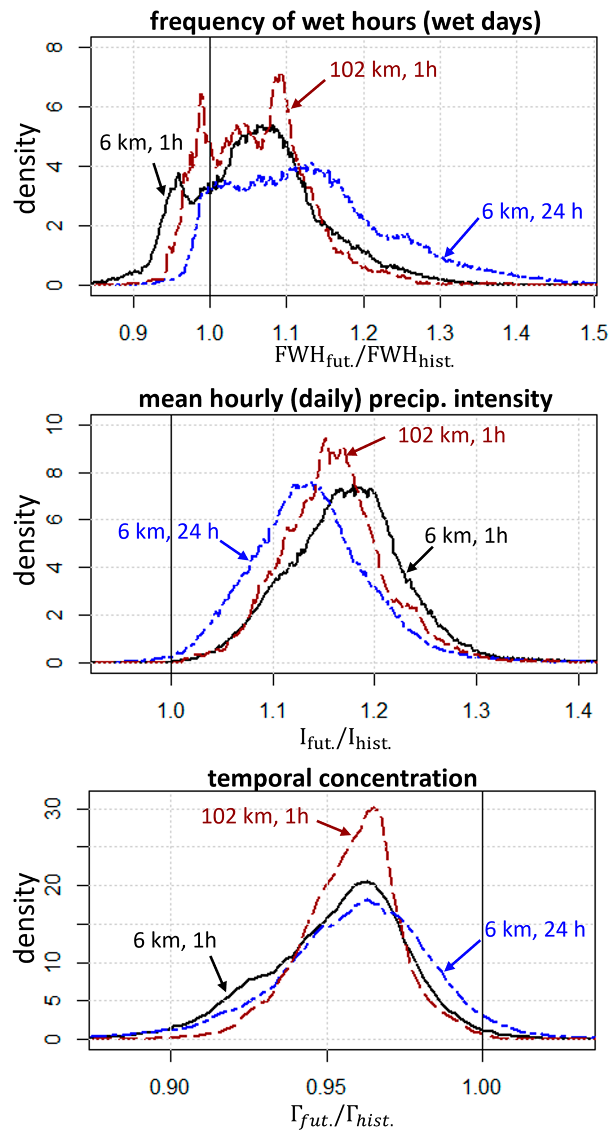


FIG. 13. Statistical distributions of change in the precipitation statistics across all the pixels of the study domain at different spatial and temporal resolutions. For each statistic, the change is expressed as the ratio of the future value over the historical value (change ratio).

and often require supplemental analyses for interpretation, spectral analysis allows to rapidly and nonparametrically detect variations and changes in the spatial and temporal structure of any climatic variable. One shall note that the utility of Fourier spectral analysis is not restricted to the analysis of narrowband signals and periodic modes of variability such as the diurnal and seasonal cycles; it can provide information about any type of signal and any form of variability, including pseudorandom or chaotic variability and the so-called "background noise" or "weather noise" (Mann and Lees 1996). Multidimensional spectral analysis also provides tools to evaluate the spatial directionality and anisotropy in precipitation features as well as their propagative properties (Guilloteau et al. 2021). These aspects were also assessed for the presently analyzed datasets; however, no salient changes were found between historical and PGW simulations (not shown), possibly due to the limitations of the PGW simulation approach. Indeed, when perturbating the historical NARR boundary conditions month by month, we preserve their day-to-day variations. Therefore, while the storms' thermodynamics show a response to the warmer and moister atmosphere, the timing of the occurrence of storms in the PGW simulations is the same as in the historical simulation. Direct downscaling of GCM simulations (McGinnis and Mearns 2021; Rahimi et al. 2024) would arguably be a more adapted approach to evaluate these other aspects of change in precipitation.

The physical drivers behind the intensification of the mean hourly precipitation rate, the increased concentration of the precipitation volume across space and time, and the increased spatial and temporal variability and "sharpness" of precipitation features are to be sought in the enhancement of the convective activity in a warmer and moister atmosphere. Higher atmospheric temperatures and greater water-holding capacity of the atmosphere allow for potentially more latent heat to be released during moist convection processes. The consequence of this is a general increase in the convective available potential energy (CAPE), leading to more widespread, and/or more intense, and/or more organized convection (Trapp et al. 2007; Prein et al. 2017; Fowler et al. 2021; Bao et al. 2024). In Chen et al. (2023), the spatial sharpening of storms at the daily temporal resolution was attributed to the intensification of updrafts within convective cores. It however remains uncertain which effect, between the increase in the spread of convection (meaning the increasing convective to stratiform precipitation ratio), the increase of the intensity of convection, and the increase in the convective organization, has more impact on precipitation statistics at different scales. While increasing convective intensity may have more impact at the submesoscale and subdaily scale, change in the degree of organization of convection is expected to have more consequences at the coarser meso and daily scales (Bao and Sherwood 2019). Future analyses of storms' structure, including the degree of convective organization, in convection-permitting simulations shall shed more light on the mechanisms driving the future changes in storms and precipitation characteristics.

In the present study, the increased spatial and temporal concentration of precipitation and sharpening of precipitation features is established from historical and PGW future simulations at the regional scale in western North America. Because the CAPE and the latent heat released during moist convection processes are expected to increase on average across the globe under global warming (Seeley and Romps 2015), the findings of the present regional study are likely to be relevant to many other regions of the world. However, beyond the thermodynamics of moist convection, many factors influencing the characteristics of precipitation are likely to also change under global warming (in particular, synoptic circulation patterns controlling the transport of water vapor), and the response of precipitation dynamics to global warming will undoubtedly vary from one region to another. Currently, the high computational cost of storm-resolving simulations at hourly resolutions does not allow for an analysis such as the one presented here to be performed globally. Storm-resolving regional simulations in other areas of the world need to be analyzed to confirm or infirm the generalizability of the present results [see e.g., the Dallan et al. (2024) study in the Alpine–Mediterranean region].

In regard to the consequences of the projected changes in terms of hydrological impacts, higher mean precipitation intensity and higher spatiotemporal concentration of precipitation naturally imply higher runoff rates and higher flood susceptibility, especially regarding flash floods in small hydrologic basins. In addition to the direct hydrological impacts, the increase of the spatiotemporal variability of precipitation at fine scales may negatively impact our capacity to produce accurate precipitation forecasts in the future, as shorter time persistence and sharper spatial gradients typically render forecasting more challenging (Germann and Zawadzki 2002). If the typical spatial and temporal dimensions of precipitation features decrease in the future, as is suggested by the decrease in the HPP and HPW statistics in the PGW simulations, the effective resolution (Wedi 2014; Bolgiani et al. 2020) of models and forecasts shall improve accordingly to maintain adequacy. We note that these considerations are also relevant when it comes to observations and observational products (Guilloteau et al. 2017; Herrera et al. 2019; Guilloteau and Foufoula-Georgiou 2020), which are used to evaluate numerical models and are also assimilated in some models.

*Acknowledgments.* Dr. Guilloteau and Prof. Foufoula-Georgiou acknowledge the support of NASA through the Precipitation Measurement Mission program (Grant 80NSSC22K0597) and the Weather and Atmospheric Dynamics program (Grant 80NSSC23K1304), as well as the support of NSF's Division of Information and Intelligent Systems through the Expand AI2ES program (Grant IIS2324008), and the support of the Samueli Endowed Chair in Engineering at the University of California Irvine. Dr. Chen and Dr. Leung are supported by the Office of Science, U.S. Department of Energy (DOE) Biological and Environmental Research as part of the HyperFACETS project funded by the Regional and Global Model Analysis and Multisector Dynamics program areas. The Pacific Northwest National Laboratory (PNNL) is operated for DOE by Battelle Memorial Institute under contract DE-AC05-76RL01830.

*Data availability statement.* The WRF historical and PGW simulation outputs have been archived at the National Energy Research Scientific Computing Center (NERSC) High Performance Storage System under/home/x/xdchen/SERDP/PNNL_WRF_wUS6km. The subset of data used in this analysis is also available via request to Dr. Chen and Dr. Leung.

## REFERENCES

Abdelmoaty, H. M., and S. M. Papalexiou, 2023: Changes of extreme precipitation in CMIP6 projections: Should we use stationary or nonstationary models? *J. Climate*, **36**, 2999–3014, https://doi.org/10.1175/JCLI-D-22-0467.1.

Alijani, B., J. O'Brien, and B. Yarnal, 2008: Spatial analysis of precipitation intensity and concentration in Iran. *Theor. Appl. Climatol.*, **94**, 107–124, https://doi.org/10.1007/s00704-007-0344-y.

Antoine, J.-P., P. Carrette, R. Murenzi, and B. Piette, 1993: Image analysis with two-dimensional continuous wavelet transform. *Signal Process.*, **31**, 241–272, https://doi.org/10.1016/0165-1684(93)90085-O.

Bao, J., and S. C. Sherwood, 2019: The role of convective self-aggregation in extreme instantaneous versus daily precipitation. *J. Adv. Model. Earth Syst.*, **11**, 19–33, https://doi.org/10.1029/2018MS001503.

——, B. Stevens, L. Kluft, and C. Muller, 2024: Intensification of daily tropical precipitation extremes from more organized convection. *Sci. Adv.*, **10**, eadj6801, https://doi.org/10.1126/sciadv.adj6801.

Berg, P., C. Moseley, and J. O. Haerter, 2013: Strong increase in convective precipitation in response to higher temperatures. *Nat. Geosci.*, **6**, 181–185, https://doi.org/10.1038/ngeo1731.

Bolgiani, P., D. Santos-Muñoz, S. Fernández-González, M. Sastre, F. Valero, and M. L. Martín, 2020: Microburst detection with the WRF model: Effective resolution and forecasting indices. *J. Geophys. Res. Atmos.*, **125**, e2020JD032883, https://doi.org/10.1029/2020JD032883.

Brogli, R., C. Heim, J. Mensch, S. L. Sørland, and C. Schär, 2023: The pseudo-global-warming (PGW) approach: Methodology, software package PGW4ERA5 v1.1, validation, and sensitivity analyses. *Geosci. Model Dev.*, **16**, 907–926, https://doi.org/10.5194/gmd-16-907-2023.

Byrne, M. P., and P. A. O'Gorman, 2015: The response of precipitation minus evapotranspiration to climate warming: Why the "wet-get-wetter, dry-get-drier" scaling does not hold over land. *J. Climate*, **28**, 8078–8092, https://doi.org/10.1175/JCLI-D-15-0369.1.

Chan, S. C., E. J. Kendon, H. J. Fowler, A. Kahraman, J. Crook, N. Ban, and A. F. Prein, 2023: Large-scale dynamics moderate impact-relevant changes to organised convective storms. *Commun. Earth Environ.*, **4**, 8, https://doi.org/10.1038/s43247-022-00669-2.

Chen, X., L. R. Leung, Y. Gao, Y. Liu, M. Wigmosta, and M. Richmond, 2018: Predictability of extreme precipitation in western U.S. watersheds based on atmospheric river occurrence, intensity, and duration. *Geophys. Res. Lett.*, **45**, 11 693–11 701, https://doi.org/10.1029/2018GL079831.

——, ——, M. Wigmosta, and M. Richmond, 2019: Impact of atmospheric rivers on surface hydrological processes in western U.S. watersheds. *J. Geophys. Res. Atmos.*, **124**, 8896–8916, https://doi.org/10.1029/2019JD030468.

——, ——, Y. Gao, Y. Liu, and M. Wigmosta, 2023: Sharpening of cold-season storms over the western United States. *Nat. Climate Change*, **13**, 167–173, https://doi.org/10.1038/s41558-022-01578-0.

Chou, C., J. D. Neelin, C.-A. Chen, and J.-Y. Tu, 2009: Evaluating the "rich-get-richer" mechanism in tropical precipitation change under global warming. *J. Climate*, **22**, 1982–2005, https://doi.org/10.1175/2008JCLI2471.1.

Cordeira, J. M., J. Stock, M. D. Dettinger, A. M. Young, J. F. Kalansky, and F. M. Ralph, 2019: A 142-year climatology of Northern California landslides and atmospheric rivers. *Bull. Amer. Meteor. Soc.*, **100**, 1499–1509, https://doi.org/10.1175/BAMS-D-18-0158.1.

Dallan, E., F. Marra, G. Fosser, M. Marani, and M. Borga, 2024: Dynamical factors heavily modulate the future increase of sub-daily extreme precipitation in the Alpine-Mediterranean region. *Earth's Future*, **12**, e2024EF005185, https://doi.org/10.1029/2024EF005185.

Daly, C., M. Halbleib, J. I. Smith, W. P. Gibson, M. K. Doggett, G. H. Taylor, J. Curtis, and P. P. Pasteris, 2008: Physiographically sensitive mapping of climatological temperature and precipitation across the conterminous United States. *Int. J. Climatol.*, **28**, 2031–2064, https://doi.org/10.1002/joc.1688.

Donat, M. G., A. L. Lowry, L. V. Alexander, P. A. O'Gorman, and N. Maher, 2016: More extreme precipitation in the world's dry and wet regions. *Nat. Climate Change*, **6**, 508–513, https://doi.org/10.1038/nclimate2941.

Dong, Q., W. Wang, K. E. Kunkel, Q. Shao, W. Xing, and J. Wei, 2021: Heterogeneous response of global precipitation concentration to global warming. *Int. J. Climatol.*, **41**, E2347–E2359, https://doi.org/10.1002/joc.6851.

Ferreira, R. N., M. R. Nissenbaum, and T. M. Rickenbach, 2018: Climate change effects on summertime precipitation organization in the Southeast United States. *Atmos. Res.*, **214**, 348–363, https://doi.org/10.1016/j.atmosres.2018.08.012.

Fowler, H. J., and Coauthors, 2021: Anthropogenic intensification of short-duration rainfall extremes. *Nat. Rev. Earth Environ.*, **2**, 107–122, https://doi.org/10.1038/s43017-020-00128-6.

Gao, Y., J. Lu, L. R. Leung, Q. Yang, S. Hagos, and Y. Qian, 2015: Dynamical and thermodynamical modulations on future changes of landfalling atmospheric rivers over western North America. *Geophys. Res. Lett.*, **42**, 7179–7186, https://doi.org/10.1002/2015GL065435.

Gastwirth, J. L., 1972: The estimation of the Lorenz curve and Gini index. *Rev. Econ. Stat.*, **54**, 306–316, https://doi.org/10.2307/1937992.

Gensini, V. A., A. M. Haberlie, and W. S. Ashley, 2023: Convection-permitting simulations of historical and possible future climate over the contiguous United States. *Climate Dyn.*, **60**, 109–126, https://doi.org/10.1007/s00382-022-06306-0.

Germann, U., and I. Zawadzki, 2002: Scale-dependence of the predictability of precipitation from continental radar images. Part I: Description of the methodology. *Mon. Wea. Rev.*, **130**, 2859–2873, https://doi.org/10.1175/1520-0493(2002)130<2859:SDOTPO>2.0.CO;2.

Gershunov, A., and Coauthors, 2019: Precipitation regime change in Western North America: The role of Atmospheric Rivers. *Sci. Rep.*, **9**, 9944, https://doi.org/10.1038/s41598-019-46169-w.

Giorgi, F., F. Raffaele, and E. Coppola, 2019: The response of precipitation characteristics to global warming from climate projections. *Earth Syst. Dyn.*, **10**, 73–89, https://doi.org/10.5194/esd-10-73-2019.

Goffin, B. D., P. Kansara, and V. Lakshmi, 2024: Intensification in the wettest days to 50 percent of annual precipitation (WD50) across Europe. *Geophys. Res. Lett.*, **51**, e2023GL107403, https://doi.org/10.1029/2023GL107403.

Guilinger, J. J., E. Foufoula-Georgiou, A. B. Gray, J. T. Randerson, P. Smyth, N. C. Barth, and M. L. Goulden, 2023: Predicting postfire sediment yields of small steep catchments using airborne lidar differencing. *Geophys. Res. Lett.*, **50**, e2023GL104626, https://doi.org/10.1029/2023GL104626.

Guilloteau, C., and E. Foufoula-Georgiou, 2020: Multiscale evaluation of satellite precipitation products: Effective resolution of IMERG. *Satellite Precipitation Measurement*, Springer, 533–558, https://doi.org/10.1007/978-3-030-35798-6_5.

——, ——, and C. D. Kummerow, 2017: Global multiscale evaluation of satellite passive microwave retrieval of precipitation during the TRMM and GPM eras: Effective resolution and regional diagnostics for future algorithm development. *J. Hydrometeor.*, **18**, 3051–3070, https://doi.org/10.1175/JHM-D-17-0087.1.

——, ——, P. Kirstetter, J. Tan, and G. J. Huffman, 2021: How well do multisatellite products capture the space–time dynamics of precipitation? Part I: Five products assessed via a wavenumber–frequency decomposition. *J. Hydrometeor.*, **22**, 2805–2823, https://doi.org/10.1175/JHM-D-21-0075.1.

——, P. V. Le, and E. Foufoula-Georgiou, 2023: Constraining the multiscale structure of geophysical fields in machine learning: The case of precipitation. *IEEE Geosci. Remote Sens. Lett.*, **20**, 1–5, https://doi.org/10.1109/LGRS.2023.3284278.

Guinard, K., A. Mailhot, and D. Caya, 2015: Projected changes in characteristics of precipitation spatial structures over North America. *Int. J. Climatol.*, **35**, 596–612, https://doi.org/10.1002/joc.4006.

Herrera, S., S. Kotlarski, P. M. Soares, R. M. Cardoso, A. Jaczewski, J. M. Gutiérrez, and D. Maraun, 2019: Uncertainty in gridded precipitation products: Influence of station density, interpolation method and grid resolution. *Int. J. Climatol.*, **39**, 3717–3729, https://doi.org/10.1002/joc.5878.

Huang, X., D. L. Swain, and A. D. Hall, 2020: Future precipitation increase from very high resolution ensemble downscaling of extreme atmospheric river storms in California. *Sci. Adv.*, **6**, eaba1323, https://doi.org/10.1126/sciadv.aba1323.

Kendon, E. J., A. F. Prein, C. A. Senior, and A. Stirling, 2021: Challenges and outlook for convection-permitting climate modelling. *Philos. Trans. Roy. Soc.*, **A379**, 20190547, https://doi.org/10.1098/rsta.2019.0547.

Koszuta, M., N. Siler, L. R. Leung, and J. J. Wettstein, 2024: Weakened orographic influence on cool-season precipitation in simulations of future warming over the western US. *Geophys. Res. Lett.*, **51**, e2023GL107298, https://doi.org/10.1029/2023GL107298.

Kunkel, K. E., T. R. Karl, M. F. Squires, X. Yin, S. T. Stegall, and D. R. Easterling, 2020: Precipitation extremes: Trends and relationships with average precipitation and precipitable water in the contiguous United States. *J. Appl. Meteor. Climatol.*, **59**, 125–142, https://doi.org/10.1175/JAMC-D-19-0185.1.

Lenderink, G., R. Barbero, J. M. Loriaux, and H. J. Fowler, 2017: Super-Clausius–Clapeyron scaling of extreme hourly convective precipitation and its relation to large-scale atmospheric conditions. *J. Climate*, **30**, 6037–6052, https://doi.org/10.1175/JCLI-D-16-0808.1.

Lebsock, M. D., and T. S. L'Ecuyer, 2011: The retrieval of warm rain from CloudSat. *J. Geophys. Res.*, **116**, D20209, https://doi.org/10.1029/2011JD016076.

Liu, C., and R. P. Allan, 2013: Observed and simulated precipitation responses in wet and dry regions 1850–2100. *Environ. Res. Lett.*, **8**, 034002, https://doi.org/10.1088/1748-9326/8/3/034002.

——, and Coauthors, 2017: Continental-scale convection-permitting modeling of the current and future climate of North America. *Climate Dyn.*, **49**, 71–95, https://doi.org/10.1007/s00382-016-3327-9.

Liu, M., G. A. Vecchi, J. A. Smith, and T. R. Knutson, 2019: Causes of large projected increases in hurricane precipitation rates with global warming. *npj Climate Atmos. Sci.*, **2**, 38, https://doi.org/10.1038/s41612-019-0095-3.

Lu, J., G. A. Vecchi, and T. Reichler, 2007: Expansion of the Hadley cell under global warming. *Geophys. Res. Lett.*, **34**, L06805, https://doi.org/10.1029/2006GL028443.

Lucas-Picher, P., D. Argüeso, E. Brisson, Y. Tramblay, P. Berg, A. Lemonsu, S. Kotlarski, and C. Caillaud, 2021:

Convection-permitting modeling with regional climate models: Latest developments and next steps. *Wiley Interdiscip. Rev.: Climate Change*, **12**, e731, https://doi.org/10.1002/wcc.731.

Mamalakis, A., and Coauthors, 2021: Zonally contrasting shifts of the tropical rain belt in response to climate change. *Nat. Climate Change*, **11**, 143–151, https://doi.org/10.1038/s41558-020-00963-x.

Mann, M. E., and J. M. Lees, 1996: Robust estimation of background noise and signal detection in climatic time series. *Climatic Change*, **33**, 409–445, https://doi.org/10.1007/BF00142586.

McGinnis, S., and L. Mearns, 2021: Building a climate service for North America based on the NA-CORDEX data archive. *Climate Serv.*, **22**, 100233, https://doi.org/10.1016/j.cliser.2021.100233.

Monjo, R., and J. Martin-Vide, 2016: Daily precipitation concentration around the world according to several indices. *Int. J. Climatol.*, **36**, 3828–3838, https://doi.org/10.1002/joc.4596.

Morrison, H., G. Thompson, and V. Tatarskii, 2009: Impact of cloud microphysics on the development of trailing stratiform precipitation in a simulated squall line: Comparison of one- and two-moment schemes. *Mon. Wea. Rev.*, **137**, 991–1007, https://doi.org/10.1175/2008MWR2556.1.

O'Gorman, P. A., 2015: Precipitation extremes under climate change. *Curr. Climate Change Rep.*, **1**, 49–59, https://doi.org/10.1007/s40641-015-0009-3.

Papalexiou, S. M., and A. Montanari, 2019: Global and regional increase of precipitation extremes under global warming. *Water Resour. Res.*, **55**, 4901–4914, https://doi.org/10.1029/2018WR024067.

Pascale, S., V. Lucarini, X. Feng, A. Porporato, and S. Ul Hasson, 2016: Projected changes of rainfall seasonality and dry spells in a high greenhouse gas emissions scenario. *Climate Dyn.*, **46**, 1331–1350, https://doi.org/10.1007/s00382-015-2648-4.

Pendergrass, A. G., 2018: What precipitation is extreme? *Science*, **360**, 1072–1073, https://doi.org/10.1126/science.aat1871.

Pfahl, S., P. A. O'Gorman, and E. M. Fischer, 2017: Understanding the regional pattern of projected future changes in extreme precipitation. *Nat. Climate Change*, **7**, 423–427, https://doi.org/10.1038/nclimate3287.

Polson, D., and G. C. Hegerl, 2017: Strengthening contrast between precipitation in tropical wet and dry regions. *Geophys. Res. Lett.*, **44**, 365–373, https://doi.org/10.1002/2016GL071194.

Prein, A. F., C. Liu, K. Ikeda, S. B. Trier, R. M. Rasmussen, G. J. Holland, and M. P. Clark, 2017: Increased rainfall volume from future convective storms in the US. *Nat. Climate Change*, **7**, 880–884, https://doi.org/10.1038/s41558-017-0007-7.

Rahimi, S., and Coauthors, 2024: An overview of the Western United States Dynamically Downscaled Dataset (WUS-D3). *Geosci. Model Dev.*, **17**, 2265–2286, https://doi.org/10.5194/gmd-17-2265-2024.

Rajah, K., T. O'Leary, A. Turner, G. Petrakis, M. Leonard, and S. Westra, 2014: Changes to the temporal distribution of daily precipitation. *Geophys. Res. Lett.*, **41**, 8887–8894, https://doi.org/10.1002/2014GL062156.

Ralph, F. M., and M. D. Dettinger, 2011: Storms, floods, and the science of atmospheric rivers. *Eos, Trans. Amer. Geophys. Union*, **92**, 265–266, https://doi.org/10.1029/2011EO320001.

Rasmussen, R. M., and Coauthors, 2023: CONUS404: The NCAR–USGS 4-km long-term regional hydroclimate reanalysis over the CONUS. *Bull. Amer. Meteor. Soc.*, **104**, E1382–E1408, https://doi.org/10.1175/BAMS-D-21-0326.1.

Rutz, J. J., W. J. Steenburgh, and F. M. Ralph, 2014: Climatological characteristics of atmospheric rivers and their inland penetration over the western United States. *Mon. Wea. Rev.*, **142**, 905–921, https://doi.org/10.1175/MWR-D-13-00168.1.

Sangüesa, C., R. Pizarro, A. Ibañez, J. Pino, D. Rivera, P. García-Chevesich, and B. Ingram, 2018: Spatial and temporal analysis of rainfall concentration using the Gini index and PCI. *Water*, **10**, 112, https://doi.org/10.3390/w10020112.

Seeley, J. T., and D. M. Romps, 2015: Why does tropical convective available potential energy (CAPE) increase with warming? *Geophys. Res. Lett.*, **42**, 10 429–10 437, https://doi.org/10.1002/2015GL066199.

Skamarock, W. C., and Coauthors, 2008: A description of the Advanced Research WRF version 3. NCAR Tech. Note NCAR/TN-475+STR, 113 pp., https://doi.org/10.5065/D68S4MVH.

Stevens, B., and Coauthors, 2019: DYAMOND: The DYnamics of the Atmospheric General circulation Modeled On Non-hydrostatic domains. *Prog. Earth Planet. Sci.*, **6**, 61, https://doi.org/10.1186/s40645-019-0304-z.

Swain, D. L., B. Langenbrunner, J. D. Neelin, and A. Hall, 2018: Increasing precipitation volatility in twenty-first-century California. *Nat. Climate Change*, **8**, 427–433, https://doi.org/10.1038/s41558-018-0140-y.

Takayabu, I., and Coauthors, 2022: Convection-permitting models for climate research. *Bull. Amer. Meteor. Soc.*, **103**, E77–E82, https://doi.org/10.1175/BAMS-D-21-0043.1.

Thackeray, C. W., A. Hall, J. Norris, and D. Chen, 2022: Constraining the increased frequency of global precipitation extremes under warming. *Nat. Climate Change*, **12**, 441–448, https://doi.org/10.1038/s41558-022-01329-1.

Trapp, R. J., N. S. Diffenbaugh, H. E. Brooks, M. E. Baldwin, E. D. Robinson, and J. S. Pal, 2007: Changes in severe thunderstorm environment frequency during the 21st century caused by anthropogenically enhanced global radiative forcing. *Proc. Natl. Acad. Sci. USA*, **104**, 19 719–19 723, https://doi.org/10.1073/pnas.0705494104.

Vallis, G. K., P. Zurita-Gotor, C. Cairns, and J. Kidston, 2015: Response of the large-scale structure of the atmosphere to global warming. *Quart. J. Roy. Meteor. Soc.*, **141**, 1479–1501, https://doi.org/10.1002/qj.2456.

VanBuskirk, O., P. Ćwik, R. A. McPherson, H. Lazrus, E. Martin, C. Kuster, and E. Mullens, 2021: Listening to stakeholders: Initiating research on subseasonal-to-seasonal heavy precipitation events in the contiguous United States by first understanding what stakeholders need. *Bull. Amer. Meteor. Soc.*, **102**, E1972–E1986, https://doi.org/10.1175/BAMS-D-20-0313.1.

Venugopal, V., and J. M. Wallace, 2016: Climatology of contribution-weighted tropical rain rates based on TRMM 3B42. *Geophys. Res. Lett.*, **43**, 10 439–10 477, https://doi.org/10.1002/2016GL069909.

Wedi, N. P., 2014: Increasing horizontal resolution in numerical weather prediction and climate simulations: Illusion or panacea? *Philos. Trans. Roy. Soc.*, **A372**, 20130289, https://doi.org/10.1098/rsta.2013.0289.

Westra, S., and Coauthors, 2014: Future changes to the intensity and frequency of short-duration extreme rainfall. *Rev. Geophys.*, **52**, 522–555, https://doi.org/10.1002/2014RG000464.

Zaitchik, B. F., M. Rodell, M. Biasutti, and S. I. Seneviratne, 2023: Wetting and drying trends under climate change. *Nat. Water*, **1**, 502–513, https://doi.org/10.1038/s44221-023-00073-w.